

A Multiple-Regime Approach to Atmospheric Zonal-Flow Vacillation

Seongjoon Koo

Dept. of Atmospheric and Oceanic Sciences
and Institute of Geophysics and Planetary Physics,
University of California, Los Angeles, CA, USA

Andrew W. Robertson *

International Research Institute for Climate Prediction,
The Earth Institute at Columbia University, Palisades, NY, USA

Michael Ghil †

Dept. of Atmospheric and Oceanic Sciences
and Institute of Geophysics and Planetary Physics,
University of California, Los Angeles, CA, USA

June 11, 2005

QJRMS, submitted

*Correspondence address: IRI - Monell 230, 61 Route 9W, Palisades, NY 10964, USA. Phone: +1 845 680 4491, Fax: +1 845 680 4865, E-mail: awr@iri.columbia.edu.

†Additional affiliation: Département Terre-Atmosphère-Océan and Laboratoire de Météorologie Dynamique de CNRS/IPSL, Ecole Normale Supérieure, Paris, France.

Abstract

Zonal-flow vacillation in an idealized two-layer, global, primitive-equation model is studied in the context of multiple regimes. The spatial structure of vertically and zonally averaged zonal-flow variability resembles that observed in the Southern Hemisphere, with dipolar anomalies centered at 40° and 60° . The probability density function (PDF) of the model's zonal flow is studied in the subspace of its two leading principal components, using kernel density estimation and a Gaussian mixture model. Both techniques reveal clear evidence of multiple flow regimes, associated with the central peak of the PDF and the two pronounced shoulders attached to it. These three features are shown to be statistically significant at the 95% confidence level against a red-noise null hypothesis.

Flow composites for the two shoulders show meteorologically significant differences from climatology and similarities with observed Southern Hemisphere flow patterns. In the low-latitude regime, the narrow jet's zonal-velocity maximum lies equatorward of the climatological mean position, while in the high-latitude regime the broad jet is sometimes bimodal and has its global velocity maximum poleward of the climatological position. Changes in low-level eddy heat flux precede those of the eddy momentum forcing that drive both the regime onset and break. This phase difference between heat and momentum fluxes suggests that baroclinic processes play an important role in the regime transitions. The dependence of the preferred regimes' zonal-jet latitudes on bottom friction shows that multiple regimes coexist in a wide range of parameter values.

Keywords: low-frequency variability; circulation regimes; bimodality; annular modes

1 Introduction

The zonally averaged zonal flow in the Southern Hemisphere (SH) exhibits pronounced low-frequency variability (LFV) on intraseasonal (Webster and Keller 1975) and interannual (Trenberth 1997) time scales. The dominant mode of the observed variability (Kidson 1988a; Hartmann and Lo 1998) exhibits an equivalent barotropic vertical structure with persistent dipolar anomalies centered near 40°S and 60°S. The term *zonal-flow vacillation* has been coined to indicate the irregular variations of the SH zonal jet.

Zonal-flow vacillation between two persistent anomalous states with irregular transitions between them, suggests the relevance of the multiple-regimes concept that originated in the work of Charney and DeVore (1979). Several attempts have been made to identify multiple regimes and bimodality associated with SH zonal-flow vacillation. Based on visual inspection of the zonal jet's position, Yoden et al. (1987) found two distinct flow regimes during the 1980–1983 austral winters, corresponding to single- and double-jet states. Akahori and Yoden (1997) studied the relationship between zonal-flow vacillation and wave breaking patterns of baroclinic eddies using an idealized model. They found bimodality in a histogram of the so-called LC index, an empirical measure of the typical latitude of wave breaking that is associated with the zonal-flow vacillation. However, no bimodality was found in a histogram of the zonal-mean flow's first principal component (PC-1). Hartmann and Lo (1998) also reported finding no bimodality in PC-1 of the zonal-mean SH flow.

Recently, Koo (2002) and Koo et al. (2003) examined the probability density function (PDF) of SH zonal-flow vacillation in the subspace of PC-1 and PC-2 of the observed zonal-mean SH flow. They reported evidence of multiple flow regimes, together with low-frequency oscillations at periods near 135 and 70 days. Consideration of PC-2 was found to be crucial in identifying multimodality. Moreover, there is mounting evidence that the persistent deviations from *zonal symmetry* of observed atmospheric LFV in both the Northern Hemisphere (NH) and SH can be well described in terms of multiple regimes (Hansen and Sutera 1986; Mo and Ghil 1987, 1988; Mechoso et al. 1991; Cheng and Wallace 1993; Kimoto and Ghil 1993a, b; Michelangeli et al. 1995; Smyth et al. 1999; Cazes et al. 2003; Robertson and Mechoso 2003). This observational evidence is also accompanied by an improved understanding of the dynamics that give rise to these multiple regimes (Legras and Ghil 1985; Benzi et al. 1986; Ghil and Robertson 2002, and further references therein).

The dynamics governing the maintenance of the *extreme* phases in zonal-flow vacillation is also relatively well understood by now. Modeling (Robinson 1991; Yu and Hartmann 1993; Koo and Ghil 2002; Kravtsov et al. 2003, 2005a) and observational (Hartmann and Lo 1998; Lorenz and Hartmann 2001, 2003) studies strongly suggest that both of the vacillation's extreme phases are maintained by the effect of the transient eddies on the zonal flow's nonlinear evolution. High-frequency, synoptic-scale eddies with a period of less than 10 days are found in these studies to play a key role in the maintenance of the persistent anomalies of the zonal flow.

Despite the advances in our understanding of the extreme phases described above, the dynamics of the *transition* phases of the vacillation remains poorly understood. For example, the origin of the initial eddy forcing that drives the zonal flow into one of the extreme phases is not clear. Nor is it known what causes these two relatively persistent phases of the vacillation to break.

The main purpose of the present paper is two-fold: (i) to document and help explain the multimodality of the zonal flow in an idealized atmospheric primitive-equations (PE) model; and (ii) to study in greater detail the transitions between the model’s high- and low-latitude jet regimes. We examine, therefore, the PDF of the zonal-mean zonal flow in the simplified setting of this PE model. Our aim is to gain an improved understanding of the underlying dynamics of the multiple regimes identified in observational SH data by Koo et al. (2003). Following Hendon and Hartmann (1985), we use a two-layer PE model, with no asymmetries in its lower boundary. This set-up also removes the potentially confusing influences of the seasonal cycle, El Niño-Southern Oscillation (ENSO), long-term trends and data inhomogeneities present in observational data. Our PE model can easily be integrated for much longer time spans than the approximately 50-year observational record available from reanalysis data. This enables us to obtain reliable statistics of the regimes and their entire evolution, from onset to break.

We employ two independent but complementary methods to ascertain multimodality in the PE model: kernel density estimation and a Gaussian mixture model. Smyth et al. (1999) have shown that the mixture model framework is a powerful tool for testing the hypothesis that a complicated atmospheric PDF can be decomposed into a mixture of simpler component distributions. Even if the data’s PDF does *not* exhibit multiple peaks (modes in statistical parlance), the underlying dynamics may still be nonlinear and give rise to irregular transitions between recurrent, quasi-stationary states. Smyth et al.’s (1999) results for NH LFV suggest that multiple flow regimes may indeed be approximated by Gaussian sub-components of the data set’s PDF. Similar results were obtained by Haines and Hannachi (1995) and by Hannachi and O’Neill (2001) in general circulation models (GCMs).

Using our PE model, we demonstrate that the statistics of the vacillation’s two extreme phases is consistent with the paradigm of multiple flow regimes. The time evolution of the vacillation is then traced in phase space as well as in physical space. Composites with respect to onset and break of the two extreme phases of the vacillation can thus be constructed in a natural fashion.

This paper is organized as follows: the numerical model is described in Sect. 2 and the multiple regimes of its zonal-mean flow are discussed in Sect. 3. In Sect. 4, we examine the time evolution of the vacillating zonal jet, with emphasis on the onset and break of the vacillation’s two extreme phases. The role of surface friction is investigated in Sect. 5 using additional sensitivity runs. A discussion of the main results follows in Sect. 6, and conclusions appear in Sect. 7.

2 Model

The model used in this study is based on the atmospheric component of Saravanan and McWilliams' (1995) coupled model and is very similar to the two-layer model of Hendon and Hartmann (1985). It is a dry PE model on a sphere. The governing equations in pressure coordinates are

$$\frac{\partial \zeta}{\partial t} = -\nabla \cdot (\zeta + f)\mathbf{V} - \mathbf{k} \cdot \nabla \times \left(\omega \frac{\partial \mathbf{V}}{\partial p} - \mathbf{F} \right), \quad (1)$$

$$\frac{\partial D}{\partial t} = \mathbf{k} \cdot \nabla \times (\zeta + f)\mathbf{V} - \nabla \cdot \left(\omega \frac{\partial \mathbf{V}}{\partial p} - \mathbf{F} \right) - \nabla^2 \left(\frac{\mathbf{V} \cdot \mathbf{V}}{2} + \Phi \right), \quad (2)$$

$$\frac{\partial \theta}{\partial t} = -\nabla \cdot (\theta \mathbf{V}) - \frac{\partial}{\partial p} (\theta \omega) + Q, \quad (3)$$

$$\nabla \cdot \mathbf{V} + \frac{\partial \omega}{\partial p} = 0, \quad (4)$$

$$\frac{\partial \Phi}{\partial p} = -\frac{R\theta}{p} \left(\frac{p}{p_o} \right)^{\frac{R}{c_p}}; \quad (5)$$

here \mathbf{k} denotes the vertical unit vector, ∇ the horizontal gradient operator, $\mathbf{V} \equiv (u, v)$ the horizontal velocity, $\zeta = \mathbf{k} \cdot \nabla \times \mathbf{V}$ the vertical component of relative vorticity, $D = \nabla \cdot \mathbf{V}$ the horizontal divergence, $\Phi \equiv gz$ the geopotential, ω the vertical velocity in pressure coordinates, θ the potential temperature, p_o the surface pressure at 1000 hPa, \mathbf{F} the mechanical forcing, and Q the thermal forcing.

The above equations are discretized in the vertical following Lorenz (1960): the two layers have the same thickness, $\Delta p = 500$ hPa, and are centered at 250 hPa and 750 hPa. Due to the homogeneous lower boundary, boundary conditions are simply $\omega = 0$ at $p = 0$ and 1000 hPa. Even though the two-level configuration is a crude representation of the atmosphere, it has been used extensively and its properties are well documented. Hendon and Hartmann (1985) and Keppenne et al. (2000), in particular, reported that a two-level global PE model can produce realistic low-frequency behavior. Simple two-layer models have also been proven useful in theoretical studies of zonal-flow vacillation (Robinson 1991, 1996; Lee and Feldstein 1996) and in the study of advanced data assimilation methods (Ghil and Todling 1996).

The model is discretized in spherical harmonics, with triangular truncation at T21. This relatively low resolution has been shown to capture the essential features of zonal-flow vacillation (Yu and Hartmann 1993) and is consistent with the simple two-level discretization

in the vertical. Comparable horizontal resolutions have been adopted in other studies of the problem at hand (Robinson 1991, 1996; Lee and Feldstein 1996).

A T21 resolution results in a discrete model with 484 degrees of freedom. This number is much higher than that for low-order models, typically with $O(10)$ or fewer degrees of freedom, whose multiple equilibria have been shown to disappear when increasing the resolution (Cehelsky and Tung 1987). In fact, our model has a horizontal resolution that is much higher than Cehelsky and Tung’s (1987) 6×6 modes, which result in 78 degrees of freedom. Our model’s $O(10^2)$ degrees of freedom are comparable in number to various estimates of the large-scale atmosphere’s attractor dimension (Ghil and Childress 1987, pp. 193–195; Lions et al. 1997). The model’s time step is equal to 1 hour and results are saved every 24 hours.

The mechanical and thermal forcing terms within each model layer are chosen as follows:

$$\mathbf{F}_i = \gamma(\nabla^2 + \frac{2}{a^2})^4 \mathbf{V}_i - \frac{\delta_{i,2}}{\tau_E} \mathbf{V}_i, \quad (6)$$

$$Q_i = \gamma(\nabla^2)^4 \theta_i - \eta(\theta_i - \theta_{e,i}); \quad (7)$$

$i = 1, 2$ denote the upper and lower model levels, at 250 hPa and 750 hPa, respectively and $\delta_{i,j}$ represents the Kronecker delta. The scale-selective damping coefficient γ is chosen to act with a time scale of 1/4 day on the highest wavenumber resolved at our T21 truncation (Saravanan and McWilliams 1995). The Earth’s radius is $a = 6.4 \times 10^6$ m and the Ekman drag time scale τ_E is set to be 3 days. The radiative relaxation coefficient η is 15^{-1} days $^{-1}$. The radiative equilibrium potential temperature θ_e is prescribed to simulate perpetual-winter conditions, as in Hendon and Hartmann (1985).

The model with the parameter values described above was run for 30000 days and the first 300 days are discarded to avoid any initial transients. This model run is described and analyzed in Sects. 3 and 4, while additional runs are studied in Sect. 5.

3 Multiple regimes in zonal-mean flow

3.1 Kernel density estimation

We begin by applying a nonparametric density-estimation technique to the PDF of the model’s zonal-mean jet. A multivariate kernel density estimator (Silverman 1986) is used to estimate the PDF of the zonally and vertically averaged zonal-wind profile from the time series of 29700 daily profiles. This method was previously used by Kimoto and Ghil (1993a, b) to identify multiple flow regimes in the NH observed winter-time circulation.

First, a 10-day low-pass filter is applied to the time series of the zonally and vertically averaged zonal wind. The 31-point nonrecursive digital filter employs Lanczos smoothing to avoid Gibbs phenomena. Empirical orthogonal function (EOF) analysis was then performed on the low-pass filtered data by diagonalizing the covariance matrix. The filtering has little effect on the resulting EOF structures, although the fraction of variance described by the two leading EOFs increases slightly.

Figure 1 shows the two leading EOFs, which account for 62.1% and 17.2% of total variance, respectively. EOF-1 exhibits dipolar variability with maxima of opposite signs centered near 40° and 60°. Its node is located at 48°, which corresponds to the position of the model’s climatological zonal jet maximum. Thus, EOF-1 represents the zonal jet’s meridional displacement from its climatological mean position. The spatial structure of EOF-1 resembles its observed SH counterpart quite closely (Kidson 1988; Hartmann and Lo 1998), in spite of our model’s high degree of idealization. The second EOF exhibits an extremum near 50°, and is thus primarily associated with a strengthening and weakening of the climatological zonal jet.

[Figure 1 near here, please]

Before discussing details of PDF estimation, we first consider data scatter in phase space and its implications for PDF estimation. Data scatter in terms of “signal” and “noise” is illustrated in Fig. 2, following Kimoto and Ghil (1993a). In Figs. 2a and b, the abscissa denotes the signal component defined by

$$\|\mathbf{x}\|_S \equiv \left(\sum_{i=1}^s c_i^2 \right)^{1/2}, \quad (8)$$

and the ordinate indicates the noise component defined by

$$\|\mathbf{x}\|_N \equiv \left(\sum_{i=s+1}^{10} c_i^2 \right)^{1/2}, \quad (9)$$

where c_i is the i -th PC; $s = 1$ in Fig. 2a and $s = 2$ in Fig. 2b. The diagonal line indicates a signal-to-noise ratio of 1. Here we have chosen to truncate the “noise” at 10 leading EOFs. These ten EOFs capture 99.99% of our model’s variance and the results in Fig. 2 are found, therefore, to be insensitive to increases in this number.

[Figure 2 near here, please]

If we take EOF-1 as the sole physical signal of zonal-mean flow variability, the majority of the data points fall into the upper triangle of Fig. 2a, where the signal-to-noise ratio is less than 1, and most of them are very close to the origin of the PC-1 axis. On the other hand, if we retain the two leading EOFs as the physical signal, as shown in Fig. 2b, the signal-to-noise ratio is substantially enhanced. Furthermore, many data points which previously lay near the climatological mean state are now away from the origin.

This result implies that if a PDF is estimated using only PC-1, as in Akahori and Yoden (1997) or Hartmann and Lo (1998), a large fraction of the data points will fall near the origin, and any bimodality that might be present in the data could be obscured by noise; see also discussion in Mo and Ghil (1988) for NH regimes. In order to avoid this situation, we proceed with PDF estimation in a two-dimensional (2-D) subspace spanned by the two leading EOFs. Including PC-3 in the “signal” does not change the data scatter in Fig. 2b substantially (not shown), so that we only retain the two leading EOFs.

As in Kimoto and Ghil (1993a) and Smyth et al. (1999), the PDF is estimated for a 2-D dataset that consists of the coefficients obtained by projecting the *unfiltered* zonally and vertically averaged zonal wind anomalies onto the low-pass filtered EOFs shown in Fig. 1. This produces time series whose length equals that of the original dataset of 29700 daily profiles. Projecting the unfiltered data onto its own EOFs was found to yield a similar PDF (not shown) but with a larger number of transient events.

We applied an adaptive version of the Epanechnikov kernel method (Kimoto and Ghil 1993a) and used Euclidean distance as a similarity measure. In our adaptive method the smoothing parameter varies according to the value of the estimated PDF at each sample point. This adaptive approach allows us to achieve more reliable estimates in the data-sparse regions that lie on the outskirts of the PDF (Silverman, 1986).

The parameter h , which controls the smoothness of final density estimates, needs to be properly specified in order to avoid spurious peaks in the PDF. An objective way to determine this parameter is least-squares cross validation (LSCV), which minimizes an estimate of the integrated square error of the PDF fit (Silverman 1986). The LSCV scores are plotted as a function of the smoothing parameter h in Fig. 3. As is often the case in LSCV, the score has a fairly broad minimum, near $h = 0.3$ and 0.4 . Both values result in similar estimates of the PDF.

[Figure 3 near here, please]

The PDF constructed with $h = 0.4$ is displayed in Fig. 4a. The estimated PDF is elongated along the PC-1 axis with an overall crescent shape, and is clearly non-Gaussian. It exhibits a central peak with two pronounced shoulders attached to it. The PDF’s extremities drop towards the negative PC-2 axis. Since EOF-2 describes a modulation in the strength of the climatological jet, this shape of the PDF is consistent with the climatological jet being weaker (negative PC-2) when the jet displacement (given by PC-1) is largest, and vice versa.

[Figure 4 near here, please]

In order to establish the statistical significance of the PDF's central peak and shoulders, we construct the null hypothesis to be a unimodal PDF with a non-Gaussian crescent shape, which matches that in Fig. 4a. Note that this provides a very conservative null hypothesis for the existence of multiple regimes, since the overall crescent shape may itself be the product of them. We describe in the Appendix a nonlinear stochastic model that generates random time series of 2-vectors that have such a PDF.

One hundred sets of random time series were generated from this model, each with the same length as the original time series. A sample PDF is then computed from each of these 100 time series, using the same kernel method with the same smoothing parameter $h = 0.4$ as in Fig. 4a. These 100 sample PDFs have the non-Gaussian crescent shape of the original PDF and often exhibit multiple peaks by chance, due to the random nature of the time series from which they are computed.

The percentage of random PDFs so generated that fall short of the PDF values shown in Fig. 4a is plotted in Fig. 4b, with regions containing values that exceed 95% shaded. Both the peak and the shoulders in Fig. 4a are significant at the 95% confidence level. Although the PDF in Fig. 4a does not show multiple distinct peaks, the significance test indicates that there are three anomalously highly populated regions along the central part of the curved ridge of the PDF. Each of the three regions contains one of the regime centroids and deviates significantly from the unimodal crescent-shaped PDF. Ridging of the PDF was found by Kimoto and Ghil (1993a) to be a characteristic of multiple regime behavior of NH observed LFV. Regions of high significance also occur near the tails of the crescent-shaped PDF, where the stochastic model—in spite of its high level of sophistication—does not capture the original PDF well [cf. Fig. 4a and Fig. 13b].

Probability density estimation, a major concern of this study, is solely based on the *recurrence* of particular flow patterns so that it does not, in principle, distinguish physically meaningful, quasi-steady, low-frequency phenomena from transient noise. As a result, transient noise that recurs frequently can also have high probability density and this may obscure inherent multiple regimes that might be present in the data. In order to examine this possibility, we consider a subset of the original data that represents quasi-stationary states.

First, the speed along the phase-space trajectory is computed for each day, using Euclidean distance between the two vectors two days apart in the 2-D phase plane shown in Fig. 4. A centered difference scheme is used to compute the speed. We then select only quasi-stationary days, whose speed lies below a prescribed value, taken to be the time mean minus one standard deviation. The resulting quasi-stationary dataset consists of 4642 days (about 16% of the total). Note that the method described above is more conservative than Mo and Ghil's (1987, 1988) use of pattern correlations to define slow change in the field of interest for a number of successive days, as shown by Vautard et al. (1988).

The PDF estimated for this quasi-stationary subset is plotted in Fig. 5, using the smoothing parameter $h = 0.4$ that was determined by the LSCV. Its general shape resembles Fig. 4a, but it exhibits three distinct PDF peaks, whose locations are very close to the peak and two shoulders in the PDF of the full dataset. This suggests that the two shoulders in Fig. 4a are the trace of two distinct PDF peaks that exist inherently in the full dataset, but are obscured by transient noise.

[Figure 5 near here, please]

3.2 Gaussian mixture model

In order to corroborate the evidence of the model’s multiple regimes, we now apply Gaussian mixture modeling (Smyth et al. 1999) to the same 2-D dataset used in Sect. 3.1. In this method, a PDF is assumed to be a linear combination of a few Gaussian component density functions, each with its own mean and covariance. Thus, a PDF can be multimodal in this more general sense, even if it exhibits only one distinct peak (Titterington et al. 1985; Hand et al. 2001). The number of component Gaussians, as well as their means and covariances, can then be computed by maximizing the log-likelihood. Unlike other clustering techniques, this method uses a consistent data-driven methodology based on cross-validated likelihood to estimate the number of clusters supported by the data.

First, we compute the cross-validated log-likelihood, following the procedures described in Smyth et al. (1999). Figure 6 shows the log-likelihood values against the number of clusters k . The likelihood curve exhibits a sharp increase from $k = 1$ to $k = 2$ and then begins to saturate as k is increased further. The deep minimum at $k = 1$ clearly indicates that a single Gaussian is least likely to represent the data set’s PDF. When we increase the maximum number of clusters from 6 to 10, the log-likelihood exhibits even more clearly the asymptotic nature of the saturation from $k = 3$ on (not shown). This behavior suggests that we are experiencing the “overfitting” of a non-Gaussian PDF by an ever larger number of Gaussian clusters.

[Figure 6 near here, please]

We choose therefore $k = 3$ as the optimal trade-off between goodness-of-fit and statistical stability of the clusters’ centroids and other parameters. The log-likelihood curve starts to flatten out at this value, which agrees with the number of distinct peaks in Fig. 5.

Given the number of clusters $k = 3$, we fit a three-component mixture model to the 2-D data set. Figure 7 shows the location of the means of the Gaussians and the standard-deviation ellipses associated with their covariance matrices. The three ellipses agree with the general

shape of the PDFs estimated by the kernel method, with a crescent shape elongated along the PC-1 axis. Two of the ellipses are mainly located on the positive and negative side of the PC-1 axis, respectively. The other ellipse is centered close to the origin, with a slight shift toward the positive PC-1 and PC-2 axes. The location of the means in Fig. 7 agree quite closely with the peaks of Fig. 5, though the two means to the left and right of the central one lie slightly further outward along the curved ridge of Fig. 5.

[Figure 7 near here, please]

3.3 Physical characteristics of the regimes

We now construct regime composites in order to examine the physical-space picture associated with the three high-density regions in Figs. 4, 5 and 7. First, the location of the regime centroids in Fig. 4a is found by using the bump-hunting algorithm of Fukunaga and Hostetler (1975); the resulting centroids are denoted by '+'. These centroids in phase space are then converted to physical-space patterns, and pattern correlations between the centroids' profiles and daily zonal-mean wind profiles are computed.

We identify recurrent *episodes* within a given regime by collecting the days whose pattern correlation with the corresponding centroid is greater than 0.8. The results are not sensitive to small changes in this threshold value. Pattern correlation is used to define regime membership in order to collect flow profiles with similar shapes, rather than similar amplitudes. This agrees with the usual meteorological intuition that a larger significance should be attached to an anomaly's spatial pattern rather than to its magnitude (Kimoto and Ghil 1993b).

Finally, regime *events* are defined by taking recurrent episodes whose duration is equal to or longer than 6 days. Thus, regime events incorporate, by definition, recurrent and persistent patterns of zonal-mean flow. Flow composites of the resulting regime events are shown in Fig. 8, revealing three distinct anomalous zonal-jet states. Almost identical profiles (not shown) are obtained when episodes shorter than 6 days are also included.

[Figure 8 near here, please]

In Regime 2, called hereafter the *low-latitude regime*, the jet is located equatorward of its climatological mean position, while in Regime 3, hereafter the *high-latitude regime*, it is located poleward of this position. Finally, in Regime 1, hereafter the *central regime*, the jet is strengthened near its climatological mean position. The low- and high-latitude regimes correspond to the shoulders near the positive and negative PC-1 axis in Fig. 4a, respectively. Thus, the composite anomalies of the two regimes reflect to a large extent the two opposite phases of EOF-1 in Fig. 1.

Although the regime composites in Fig. 8 might suggest a single zonal jet shifting meridionally, careful inspection of the zonally and vertically averaged zonal flow on a daily basis reveals the occurrence of double jets during the high-latitude regime (not shown). These double jets are especially clear and more frequently observed at the upper level. Figure 9 shows the zonal-mean wind at each level composited with respect to the low- and high-latitude regime events.

[Figure 9 near here, please]

At the upper level, the high-latitude regime exhibits a broad profile with evidence of a double jet (Fig. 9b), while a single jet with strong meridional shear characterizes the low-latitude regime (Fig. 9a). Contrasts in vertical shear between the two regimes are also apparent in the figure. The zonal-flow vacillation in our model is thus not characterized simply by the meridional displacement of a single jet, but by more complex changes in the meridional wind profile that are often associated (see also Fig. 11 below) with transitions between single- and double-jet states.

4 Time evolution of zonal-flow vacillation

4.1 Model diagnostics and compositing procedures

The essence of zonal-flow vacillation can be described in the quasi-geostrophic, zonally averaged equations on a β -plane:

$$\frac{\partial \bar{u}}{\partial t} = f_o \bar{v} - \frac{\partial}{\partial y} (\overline{u'v'}) + \bar{F}, \quad (10)$$

$$\frac{\partial \bar{\theta}}{\partial t} = -\bar{\omega} \frac{\partial \Theta}{\partial p} - \frac{\partial}{\partial y} (\overline{v'\theta'}) + \bar{Q}, \quad (11)$$

$$f_o \frac{\partial \bar{u}}{\partial p} = \hat{R} \frac{\partial \bar{\theta}}{\partial y}, \quad (12)$$

where an overbar denotes a zonal average and a prime indicates a deviation from the zonal average. Such a deviation may be associated with a planetary-scale, quasi-stationary wave or with synoptic- and smaller-scale, traveling eddies; still it is often referred to as the “eddy component” of the flow and we shall do so below, except in Sect. 6. The zonal-average

mechanical forcing \overline{F} is dominated by surface friction [see Eq. (6)]; \overline{Q} is the zonal-average thermal forcing [Eq. (7)], $\Theta = \Theta(p)$ the reference potential temperature, and $\hat{R} = (p/p_o)^\kappa R/p$ the normalized gas constant.

For a given mechanical forcing \overline{F} , the zonal momentum Eq. (10) states that zonal wind is driven by the Coriolis acceleration due to meridional motion and by the meridional convergence of westerly eddy momentum flux. If Eq. (10) is vertically averaged using the upper and lower boundary conditions, the Coriolis acceleration term vanishes and the eddy momentum flux convergence becomes the *only* driving forcing of the zonal-flow vacillation against the frictional drag. For a given thermal forcing \overline{Q} , potential temperature is controlled by two competing terms in the thermodynamic Eq. (11): the adiabatic cooling/heating term associated with vertical motion and the eddy heat flux convergence/divergence term due to meridional temperature advection by eddies. The thermal-wind Eq. (12) links the dynamics governed by Eq. (10) and the thermodynamics controlled by Eq. (11). Equations (10)–(12) are now used to examine the dynamics of the low- and high-latitude regimes.

In order to investigate the time evolution of the model’s zonal-flow vacillation, composites for the two extreme phases of the vacillation were constructed. First, days belonging to either a low- or high-latitude regime event are numbered consecutively, e.g. $[1, 2, \dots, n]$, and then normalized to constitute a closed time interval of $[0, 10]$. The choice of this standardized event duration of 10 days is motivated by the average durations of the low- and high-latitude regime events, which are 10.2 and 10.1 days, respectively. The days corresponding to the standardized times $t = 0$ and $t = 10$ days are defined to constitute the regime’s onset and break, respectively. The actual data points within the standardized time interval $[0, 10]$ are interpolated for each event to 11 equidistant points, using cubic spline interpolation. Note that the actual signals at regime onset and break are not affected by this interpolation.

We now collect days before the onset and after the break, selecting the same number of days before and after as the duration of the specific regime event itself. The same normalization and interpolation techniques are applied to these two time intervals on either side of the regime, resulting in the standardized time intervals of $[-10, 0]$ and $[10, 20]$. By combining these three intervals, we have the temporal evolution of a regime event for the normalized time interval $[-10, 20]$, in increments of 1 normalized day.

The above procedures are repeated for all 277 and 289 events of the low- and high-latitude regimes, respectively. Composites of key physical variables are made for these events with respect to the standardized time interval of $[-10, 20]$. In the following subsection, we only show the interval $[-4, 14]$ for clarity. The method described above provides a very compact view of the entire evolution of the regimes, from onset to break, in a single figure. The effect of the normalization is to shrink the longer events and stretch the shorter ones, uniformly over the $[-10, 20]$ day range. We have verified that composites computed with respect to regime onset and break without the scaling described above (not shown) yield very similar results to those reported in the following.

4.2 Onset, maintenance, and break

Figure 10 shows anomaly composites of key variables with respect to the standardized regime evolution for the low- (left panels) and high-latitude (right panels) regimes. Shaded regions are statistically significant at the 95% level by a two-sided pointwise t -test. Panels (a) and (b) show the vertically averaged zonal mean wind and clearly demonstrate the dipolar nature of the zonal-flow variability centered at 40° and 60° , consistent with Fig. 8b and previous SH observations. The low-latitude regime exhibits less variability within the regime itself than the high-latitude regime, resulting in a near steady state.

[Figure 10 near here, please]

In order to measure the rate of changes in the zonal-wind profile shown in Figs. 10a and 10b, we compute the root-mean-square (RMS) difference between two meridional profiles two days apart, using a centered difference scheme, and divide it by the time interval elapsed. The quantity so obtained is a measure of the acceleration (or deceleration) of the zonal mean wind, and equivalent to the speed along the model's phase-space trajectory; see Legras and Ghil (1985) for a barotropic NH model, Vautard (1990) for NH observations, and Kondrashov et al. (2005) for a baroclinic global model. The composites of this acceleration with respect to standardized regime evolution are shown in Fig. 11.

[Figure 11 near here, please]

A similar picture (not shown) is obtained by compositing the phase-space trajectory's speed, in the 2-D phase plane spanned by the two leading EOFs shown in Fig. 1. This similarity bears out further the fact that the two leading PCs do indeed constitute the signal, as suggested by the results in Fig. 2.

During its maintenance phase, the low-latitude regime exhibits a lower RMS acceleration than the high-latitude regime. This is consistent with Figs. 10a and b, which show that the high-latitude regime has a tendency to amplify with time, while the low-latitude regime remains very constant in amplitude.

As expected, the onsets and breaks are relatively abrupt. The onsets are similarly rapid for both the low- and high-latitude regimes. On the other hand a slower change is observed for the low-latitude regime's break, while an abrupt break is clear for the high-latitude regime.

The statistical significance of the asymmetry between the breaks of the low- and high-latitude regimes is tested in the following way. First, we collect the RMS zonal-wind acceleration of the 277 low-latitude regime breaks and the 289 high-latitude regime breaks. The 566 samples are then randomly shuffled one hundred times. For each random shuffling, composites of 277

and 289 samples are computed, resulting in 100 sets of the sample means. Finally, the lower 5% and upper 95% values of these 100 sets are compared with the composites of the RMS accelerations associated with the low- and high-latitude regime breaks. The asymmetry between the breaks of the two regimes is found to be significant at the 95% level. Similarly, the asymmetry between the onset and the break of the low-latitude regime is also found to be significant at the 95% level.

Figures 10c and d depict the vertical shear of the zonal mean wind, which is closely related to the horizontal temperature gradient through the thermal-wind balance. The anomalies near 40° and 60° , which correspond to zones of anomalous baroclinicity, are roughly in phase with the anomalies in the vertically averaged zonal mean wind. Amplification of the vertical shear with time is seen in the high-latitude regime. Panels (e) and (f) of Fig. 10 show anomalies of vertically averaged eddy momentum flux convergence, i.e. the forcing of the zonal mean wind [see Eq. (10)]. The in-phase nature of the barotropic zonal mean wind anomalies and the eddy momentum flux convergence demonstrates that the eddy momentum forcing acts to maintain the anomalous position of the jet against surface friction, consistent with previous studies (Robinson 1991; Yu and Hartmann 1993; Hartmann and Lo 1998).

At the time of regime onset, anomalously strong eddy momentum forcing is observed for both regimes, consistent with the abrupt changes in zonal-mean flow observed in Fig. 11. It tends to decrease slowly thereafter during the low-latitude regime composite, while the high-latitude composite eddy-forcing retains its amplitude and drifts northward. There are large asymmetries between the regimes near the break. In the case of the low-latitude regime, the eddy momentum forcing anomalies become very small, consistent with the low RMS zonal-wind acceleration at the break shown in Fig. 11. The high-latitude regime break, on the other hand, is accompanied by a poleward shift of the negative eddy momentum forcing anomalies from the mid-latitudes. This feature is associated with the more rapid termination of the high-latitude regime.

Panels (g) and (h) of Fig. 10 show the low-level eddy heat flux. Prior to regime onset, strong positive anomalies in the eddy heat flux are observed at the central latitudes of both regimes. They are followed by eddy momentum forcing anomalies (Figs. 10e and f) and thus by abrupt acceleration of zonal mean wind anomalies at the time of regime onset (Fig. 11). This demonstrates the baroclinic nature of the eddies that drive the zonal-mean wind anomalies. The temporal lag between the evolution of the eddy heat flux and the eddy momentum flux convergence, on the one hand, and the near-simultaneous occurrence of changes in the eddy momentum forcing and zonal wind acceleration, on the other, are consistent with the dynamical picture suggested by the studies discussed in Sect. 1. In this picture, equatorward propagation of baroclinic eddies and subsequent eddy-mean-flow interactions lead to eddy momentum forcing that accelerates the upper-level zonal-mean flow.

As mentioned in Sect. 1, the reinforcement of the anomalous zonal flow by the convergence of transient eddy momentum fluxes contributes to the persistence of zonal-wind anomalies during the extreme phases of the vacillation. In the context of the model regimes, the

idealized feedback argument runs as follows: upon an initial eddy momentum forcing, the zonal-mean wind starts to accelerate near 40° and 60° for the low- and high-latitude regime, respectively. The stronger eddy momentum forcing at the upper level and the deceleration of the low-level flow by surface friction lead to differential acceleration in the vertical. The enhanced vertical shear feeds baroclinic instability that generates baroclinic eddies. The resulting eddies propagate preferentially equatorward due to the sphericity of the earth, and associated eddy–zonal-mean flow interactions lead to an eddy momentum flux convergence at the upper level, closing the feedback loop.

The low-level eddy heat flux in Figs. 10g and h shows a distinct asymmetry between the low- and high-latitude regime. The low-latitude regime displays dipolar anomalies centered at 40° and 60° . The positive eddy heat flux anomalies along 40° persist until standardized epoch $t = 7$ days, at which time they begin to attenuate (Fig. 10g); this is consistent with a similar behavior of the eddy momentum forcing at 40° (Fig. 10e). The high-latitude regime, on the other hand, shows very weak positive anomalies at 60° throughout the event, while strong negative anomalies dominate in mid-latitudes (Fig. 10h). These negative anomalies extend poleward, nearly up to 60° , and increase in magnitude until the regime break; this is consistent with the poleward shift in eddy momentum forcing near the high-latitude regime break (Fig. 10f). For both the low- and high-latitude regimes, the changes in the low-level eddy heat flux near the regime break (Figs. 10g and h) precede those of eddy momentum forcing (Figs. 10e and f) by one normalized day or so, as in the case for the regime onset.

5 Dependence on surface friction

Surface friction plays an important role in regime maintenance, balancing anomalous eddy momentum forcing [see Eq. (10)]. In order to examine further the influence of surface friction on zonal-flow vacillation, six additional runs were carried out, all having the same length of 30000 days as the control run. All parameter values were held fixed in the seven runs except for the Ekman drag time scale τ_E , which controls the strength of the frictional bottom drag [see Eq. (6)]. The seven values of τ_E were 1.0, 1.5, 2.0, 2.5, 3.0 (control), 4.0 and 8.0 days.

Bivariate PDFs of the zonally and vertically averaged zonal-wind profiles were constructed for each of the seven runs, as described in Sect. 3. The precise locations of the peaks and shoulders were obtained using the bump-hunting algorithm, in the subspace of the two leading EOFs. Depending on the parameter value τ_E , we identified one, two or three zonal-flow regimes. As in Sect. 3, we collected data points that have pattern correlations of 0.8 or higher with the regime centroids in physical space, and computed the corresponding composite profiles of zonally and vertically averaged zonal wind.

The resulting latitudinal positions of the zonal-jet maxima are plotted relative to the reciprocal Ekman drag time scale $1/\tau_E$ in Fig. 12. For an intermediate range of bottom-friction values of $1.5 \text{ days} \leq \tau_E \leq 4 \text{ days}$, multiple zonal-jet regimes coexist. The zonal jet’s lati-

tudinal position and its intensity jump irregularly from one regime to another within this range. For the smallest or largest values of surface drag, only one zonal-jet regime obtains. Figure 12 thus agrees with Akahori and Yoden’s (1997) result that the bimodality of their LC index depends on the surface drag.

[Figure 12 near here, please]

Surface friction is found to have a substantial impact on the zonal-mean flow. The run using the lowest drag (highest value of τ_E) exhibits stronger and more agitated flows than the control run; there is decreased power in the ultra low-frequency band (period $T > 60$ days) and increased power in the higher-frequency band of the zonal flow’s power spectrum (not shown). Overall, lower drag values yield zonal jets that are displaced further poleward. Robinson (1997) showed that this poleward shift of the barotropic jet is consistent with the changes in the meridional structure of the eddy momentum fluxes that force it.

On the other hand, the highest-drag run shows weaker flows with reduced high-frequency variability and enhanced low-frequency variability of the zonal-mean flow. This behavior is consistent with Robinson’s (1996) result that the enhanced baroclinicity due to increased surface drag leads to more persistent zonal jets. These jets arise from the stronger feedback between the high-frequency eddies and the zonal-mean flow.

6 Discussion

The asymmetry between the regime breaks is reminiscent of the early concept of a NH zonal-index cycle (Rossby and Willett 1948; Namias 1950). These authors described the index cycle as a relaxation oscillation, with slow transitions from low to high index and fast transitions from high to low index. Willett (1948) found that the low- and high-index phases of the NH jet are associated with latitudinal shifts of the jet, as well as with changes in its intensity. Thus, they would correspond, very roughly, to our low- and high-latitude regimes, respectively. Although the importance of the index cycle in the NH has been criticized (e.g., Wallace and Hsu 1985), there has been a recent resurgence of interest in the zonally symmetric mode of variability in the NH (Thompson and Wallace 2000; Thompson et al. 2000). Wallace (2000) has drawn further attention to the connections between a zonally symmetric seesaw or “annular mode” and the North Atlantic Oscillation (NAO); see also Mo and Ghil’s (1988) “North–South oscillation,” their Fig. 10d, as well as the sectorial and hemispheric features of Keppenne et al.’s (2000) 70-day oscillation. Vallis et al. (2004) have carried out a model study in which both the NAO and an annular mode could be attributed to the same type of interaction between nonlinear dynamics and a red-noise forcing, with differing spatial characteristics.

Depending on the strength of bottom friction, we found one, two or three zonal-flow regimes,

with multiple regimes present for the Ekman drag time scale τ_E between 1.5 and 4.0 days (Fig. 12). In this parameter range, the time evolution of the zonal jet is characterized by irregular jumps from one regime to another. Model simulations that used higher drag values tend to exhibit reduced high-frequency variability of zonal jets. This is consistent with Robinson’s (1996) conclusion that the enhanced baroclinicity due to increased surface drag leads to more persistent zonal jets, as the feedback between the high-frequency eddies and the zonal flow becomes stronger. Overall, lower-drag runs yield stronger zonal jets that are displaced further poleward.

The dependence of flow regime on bottom drag and the coexistence of multiple regimes in Fig. 12 is reminiscent of the *S*-shaped bifurcation curves that arise from back-to-back saddle-node bifurcations; see, for instance, Figs. 6.5 and 10.6 in Ghil and Childress (1987). The details of the bifurcations have been worked out by Koo and Ghil (2002) in a low-order model that combines certain features of the Lorenz (1963) and Reinhold and Pierrehumbert (1982) models, but without the topography of the latter. These bifurcations lead from multiple equilibria on to periodic, quasi-periodic and chaotic solutions. The Koo and Ghil (2002) quasi-geostrophic model exhibits many of the detailed features of the observations (Koo et al. 2003) and of the high-resolution PE model results described herein. Still, according to the methodology of hierarchical modeling (Ghil and Robertson 2000), it remains to further confirm the details of the bifurcation tree by using models of a complexity and realism that lead all the way up to GCMs.

We have presented evidence of multiple regimes associated with opposite phases of zonal-flow vacillation in our idealized flat-bottom PE model. Clearly these regimes cannot be explained by the theories of multiple flow equilibria that emphasize the role of topography (Charney and DeVore 1979; Charney and Straus 1980; Benzi et al. 1986; Ghil and Childress 1987, Ch. 6).

Kravtsov et al. (2003, 2005a) have studied zonal-flow vacillation in a baroclinic β -channel model without topography. Their model, however, did include lower-boundary forcing in the form of thermal land-sea contrast. In their model, the bimodality is due to nonlinear interactions between equivalent-barotropic, stationary modes and propagating, planetary-scale modes. The stationary modes characterizing the low- and high-latitude jet states of these authors are found to be nonlinear free modes, in that their self-interaction is small, so that they do not exchange energy with the time-mean flow. This nonlinear selection explains their dominance at low frequencies. The synoptic eddies provide an important stochastic forcing that supplies energy to these modes, but play only a modest role in determining the relative persistence of the two states. Similar findings are reported by Vallis et al. (2004) in their barotropic-model study, in which the synoptic eddies are parameterized as a red-noise forcing of selected wave numbers.

In contrast to our results in which the two jet states exhibit similar persistence, Kravtsov et al.’s (2005a) high-latitude state is much more persistent than the low-latitude one. In the work of Kravtsov et al. (2003, 2005a), anomalous generation of synoptic eddies and the associated eddy feedback on the mean flow is restricted to unrealistically high values of the

surface friction (very low values of the Ekman drag time scale).

There is therewith, still, some lack of consensus on two topics associated with zonal-flow vacillation: (i) the exact role of the synoptic-scale transient eddies and the importance of active feedback between these eddies and the mean flow; and (ii) the importance and dynamical nature of annular modes in NH LFV. The exchange between Robinson (2004) and Cash et al. (2004), following up on the work of Vallis et al. (2004), illustrates the remaining open issues concerning the second point. Kravtsov et al. (2005b) provide further observational evidence for and diagnostic insight into the role of annular modes in the NH.

Concerning the first point, the work of Koo and colleagues (Koo 2002; Koo and Ghil 2002; Koo et al. 2003; and the present paper) supports the results of previous studies (Yu and Hartman 1993; Robinson 1996, 1997, 2000; Feldstein and Lee 1998) on the importance of the synoptic-eddy feedback and its dependence on lower-surface drag, although the dynamic model of Koo and Ghil (2002) only includes a few large-scale waves.

The work of Kravtsov et al. (2003, 2005a) and of Vallis et al. (2004) seems, however, to emphasize the role of barotropic nonlinearities, with synoptic eddies merely playing the role of a noninteractive, or weakly interactive, supplementary energy source for zonal-flow oscillation. These discrepancies are also reflected in differences between the bifurcation tree of Fig. 12 here vs. those of Koo and Ghil (2002) and Kravtsov et al. (2005a), respectively.

Farrell and Ioannou (2003) provide yet another perspective on the issue of eddy–mean-flow interaction and its contribution to the multimodality of the turbulent jets. Further investigations, based on observational as well as on hierarchical modeling studies (Ghil and Robertson, 2000), are thus required to resolve the role of barotropic vs. baroclinic processes, as well as that of lower-boundary forcing, whether topographic or thermal, in the phenomenology and mechanisms of zonal-flow vacillation.

An additional reason for such investigations is provided by the enhanced predictability of the extreme phases of zonal-flow vacillation. Given the long periods found in the observations, of 70 and 135 days (Koo 2002; Koo et al. 2003), a small but significant fraction of low-frequency variability in the SH could be predicted several tens of days in advance (Ghil and Robertson 2002; Koo et al. 2003).

7 Concluding remarks

7.1 Multiple regimes and their key properties

In the present paper, we have investigated zonal-flow vacillation in a two-layer global primitive-equation (PE) model. This vacillation is characterized mainly by irregular fluctuations in

the meridional position of the zonal jet. In spite of its high degree of idealization, our model simulates well the observed meridional structure of zonal-flow variability in the SH, with equivalent-barotropic anomalies of opposite signs centered at 40° and 60° .

Motivated by previous studies of multiple regimes, we have applied two advanced density estimation techniques, the kernel method and Gaussian mixtures, to model simulations of the zonally and vertically averaged zonal wind. In order to obtain results with high statistical significance, we used simulations that are 30000 days long. The kernel method shows that the PDF in the phase subspace spanned by the two leading EOFs of the zonal wind field is crescent-shaped, with a central peak and two pronounced shoulders on either side (Fig. 4). Restricting the analysis to a quasi-stationary data subset of 4642 days (about 16% of the total), when the phase-space trajectory has slower speeds, yields three small, yet distinct, PDF peaks (Fig. 5).

The statistical significance of the features in Fig. 4 was addressed by generating a null-hypothesis synthetic dataset based on a bivariate red-noise process, whose PDF approximates the crescent shape of Fig. 4. This PDF was constructed using a nonlinear stochastic model. All three peaks were shown to be statistically significant at the 95% confidence level against this fairly elaborate null hypothesis. The fact that a *nonlinear* stochastic model is needed to approximate the crescent-shaped PDF of the data provides further evidence that the underlying dynamics is nonlinear indeed. This conclusion is consistent with the mixture model results, which clearly indicate that a single Gaussian process is extremely unlikely to have generated the PDF of the data; the mixture model results also provide independent evidence for three underlying clusters (Figs. 6 and 7).

We have thus provided strong evidence of nonlinearity and multiple flow regimes in the two-layer model's zonal-flow vacillation, even in the absence of pronounced multiple peaks in the PDF of the long (30000-day) simulation. Statistical multimodality is not a necessary condition for multiple regimes. It is not a sufficient one either since, for example, a bimodal histogram can also be produced by projecting a simple closed orbit, such as the solution of a harmonic oscillator, onto one axis. Our results, based as they are on several methodologies, do support a multiple-regime description of the zonal-flow vacillation and the need for nonlinear dynamics to generate these three regimes.

As discussed in Sect. 1, bimodality or multiple regimes in zonal-mean flow were found neither by Akahori and Yoden (1997) in a simple global circulation model nor by Hartmann and Lo (1998) in SH observations. Koo et al. (2003), however, did find evidence of multiple regimes in the SH observations. This major difference in results appears to be due to the fact that our analysis—in Koo et al. (2003), as well as in the present study—was performed in a 2-D phase subspace using a kernel density estimator, while previous studies relied on one-dimensional (1-D) histograms. The analysis of the signal-to-noise ratio in the model simulation (Fig. 2) demonstrates the necessity of signal description in the 2-D subspace spanned by the two leading EOFs. We have verified that a similar PDF estimation in a 1-D subspace, using PC-1 only, does not yield strong evidence of either bimodality or multiple regimes. These results are consistent with those of Mo and Ghil (1988), who showed that inhomogeneity of

a PDF, i.e. deviations from Gaussianity, can be detected more easily in a multi-dimensional space when the peaks and shoulders of the PDF are not located on the PC-1 axis, as shown in Fig. 4a (see also Kimoto and Ghil 1993a).

Flow composites associated with the regime centroids capture three distinct zonal-jet states. A strong jet near its climatological mean position is associated with the central peak in the PDF. The two PDF shoulders—or additional peaks, depending on the dataset and estimation method—have the jet maximum located equatorward (*low-latitude regime*) or poleward (*high-latitude regime*) of its climatological position. The high-latitude regime is found to be associated with a double jet at the upper level, while the low-latitude regime is characterized by a strong single jet with enhanced meridional shear (Figs. 8 and 9). This asymmetry in jet structure suggests that zonal-flow vacillation does not simply involve meridional shifts in the jet’s position and changes in its intensity, nor is it a manifestation of linear oscillations about the climatological mean jet.

7.2 Standardized evolution of regime events

To investigate the temporal evolution of the vacillating zonal jet, we restricted our attention to persistent regime events that last 6 days or longer. Consistent with some of the previous studies (see Sect. 6), we found that baroclinic eddies act to maintain both zonal-flow regimes via weakening or strengthening of the poleward transfer of westerly momentum from lower latitudes. The high correlation between the zonal-wind anomalies and the eddy momentum forcing anomalies suggests a substantial feedback between the two (see Fig. 10). The model’s high-latitude regime tends to amplify with time, accompanied by increasing vertical shear and strengthening eddy momentum fluxes that tend to drift northward. The tendency toward poleward drift was noted by Lorenz and Hartmann (2001), though it is only seen in the high-latitude regime in our model results, and only in the eddy momentum flux. Lorenz and Hartmann (2001) interpret this drift to be a consequence of preferential equatorward propagation of baroclinic eddies due to the earth’s sphericity.

The eddy momentum forcing at regime onset is preceded by anomalous low-level eddy heat flux, consistent with previous studies (Lee and Feldstein 1996; Feldstein and Lee 1996; Robinson 2000). Eddy heat flux changes lead those in eddy momentum flux convergence by about 1 or 2 normalized days, while changes in eddy momentum forcing and zonal wind acceleration occur simultaneously. These lead-lag relationships are consistent with a dynamical picture in which equatorward propagation of baroclinic eddies and subsequent eddy–mean-flow interactions lead to eddy momentum forcing that accelerates the upper-level zonal-mean flow.

The onsets are found to be abrupt for both regimes (Fig. 11). The breaks, however, show a significant asymmetry between the two regimes: the break is abrupt for the high-latitude regime, while it is more gradual for the low-latitude regime. The eddy momentum flux convergence that forces the zonal-mean flow exhibits a similar asymmetry between the two

regime breaks (Figs. 10e and f). The low-latitude regime break is accompanied by a collapse of the momentum flux convergence at the key latitude of 40° (Fig. 10e), while the high-latitude regime break appears to be driven by the shift of negative forcing anomalies from 40° to 50° (Fig. 10f). Changes in the low-level eddy heat flux near regime break also precede those of the eddy momentum forcing, as in the case of the regime onset. Baroclinic processes appear thus to be important for both regime onset and regime break.

Acknowledgments. We would like to thank Dr. R. Saravanan for providing his atmospheric model, which became the basis of the model used in this study. Fruitful discussions with Drs. S. Feldstein, K. Ide, M. Kimoto, and S. Kravtsov are gratefully acknowledged. An earlier version of the manuscript benefited substantially from a careful review by Dr. W. Robinson. This research was supported by NSF Grant ATM00-81231 (MG and SK), and DOE Grant DE-FG03-98ER62615 (AWR).

Appendix: A stochastic model to test statistical significance of the PDF

In Sect. 3.1, we assess the statistical significance of the three distinct features of the PDF in Fig. 4a. The null hypothesis postulated is a unimodal PDF with the non-Gaussian crescent shape of the deterministic model simulation's PDF. In order to generate random time series of 2-vectors that have such a PDF, we construct a nonlinear stochastic model based on a 2-D Langevin equation (Kloeden and Platen 1992):

$$\begin{pmatrix} dx \\ dy \end{pmatrix} = -\beta \begin{pmatrix} \frac{\partial V}{\partial x} \\ \frac{\partial V}{\partial y} \end{pmatrix} dt + \epsilon^{1/2} \begin{pmatrix} dW_1 \\ dW_2 \end{pmatrix}. \quad (\text{A1})$$

Here V is a potential function that determines a mean drift (deterministic forcing) via its gradient, and $d\mathbf{W} = (dW_1, dW_2)$ is a 2-D Wiener process with two independent components. Each component of $d\mathbf{W}$ has zero mean and variance equal to dt . The two parameters β and ϵ determine the strength of the two competing terms on the right-hand side, that is, mean drift and diffusion.

We derive the potential function V from the deterministic model's simulated flow history such that the asymptotic solution of Eq. (A1) has a unimodal crescent-shaped PDF. To obtain such a form, we let

$$V = -\frac{\epsilon}{2} \log P^*, \quad (\text{A2})$$

where P^* is a very strongly smoothed PDF of the deterministic model data. This P^* is chosen so as to yield the unimodal distribution that is closest to the one in Fig. 4a, but before any sign of the multimodality appears in the distribution. The logarithmic functional form in Eq. (A2) is motivated by the solution of the Fokker-Planck equation corresponding to Eq. (A1). The same approach has been used by Hansen and Sutera (1995) in the context of a 1-D problem. Figure 13a shows the resulting potential function. Note that this functional form of $V(x, y)$ is not likely to be a linear function of x and y . Making $V(x, y)$ a quadratic polynomial in x and y (such as concentric ellipses) would yield a linear model (by Eq. (A1)).

[Figure 13 near here, please]

The two parameters β and ϵ in Eq. (A1) are chosen so as to generate a random time series of 200 000 samples whose PDF is as close as possible to the highly smoothed PDF P^* and whose decorrelation times are equal to those of the deterministic model's output. The random time series is obtained by numerically solving the stochastic differential equation (A1) using the Euler method (Kloeden and Platen 1992). The decorrelation times are defined by

$$T^{(x)} = \int_{-t_1}^{+t_1} \rho^{(x)}(t) dt, \quad (\text{A3})$$

$$T^{(y)} = \int_{-t_2}^{+t_2} \rho^{(y)}(t) dt, \quad (\text{A4})$$

where $\rho^{(x)}(t)$ and $\rho^{(y)}(t)$ are the autocorrelations of PC-1 and PC-2 time series at lag t , and t_1 and t_2 are approximate zero-crossing times, chosen to be 70 days and 35 days, respectively. The decorrelation times of the deterministic model output are $T^{(x)} = 44$ days and $T^{(y)} = 17$ days.

Under these constraints, the model parameter values are given by $\beta = 0.21$ and $\epsilon = 3.20$ with time step $\Delta t = 0.15$ days. Slight differences, less than 10%, in variance of simulated time series from that of the deterministic model output are adjusted before any PDF estimations, so that both the simulated and original time series have the same variance. Figure 13b shows the asymptotic PDF estimated from the simulated time series of 200 000 samples by Eq. (A1). This estimated PDF is unimodal and has the general crescent shape of the PDF shown in Fig. 4a.

References

- Akahori, K., and S. Yoden, Zonal flow vacillation and bimodality of baroclinic eddy life cycles in a simple global circulation model, *J. Atmos. Sci.*, 54,

2349–2361, 1997.

- Benzi, R., A. Speranza, and A. Sutera, A minimal baroclinic model for the statistical properties of low-frequency variability, *J. Atmos. Sci.*, *43*, 2962–2967, 1986.
- Cash, B. A., Kushner, P. J., Vallis, G. K., Reply, *J. Atmos. Sci.*, *61*, 954–956, 2004.
- Cazes, G., A. W. Robertson, and C. R. Mechoso, Seasonal dependence of teleconnections over South America. *J. Climate*, *16*, 1159–1176, 2003.
- Cehelsky, P., and K. K. Tung, Theories of multiple equilibria and weather regimes—A critical reexamination. Part II: Baroclinic two-layer models, *J. Atmos. Sci.*, *44*, 3282–3303, 1987.
- Charney, J. G., and J. G. DeVore, Multiple flow equilibria in the atmosphere and blocking, *J. Atmos. Sci.*, *36*, 1205–1216, 1979.
- Charney, J. G., and D. M. Straus, Form-drag instability, multiple equilibria and propagating planetary waves in baroclinic, orographically forced, planetary wave systems, *J. Atmos. Sci.*, *37*, 1157–1176, 1980.
- Cheng, X., and J. M. Wallace, Cluster analysis of the Northern Hemisphere wintertime 500-hPa height field: Spatial patterns, *J. Atmos. Sci.*, *50*, 2674–2696, 1993.
- Farrell, B. F., and P. J. Ioannou, Structural stability of turbulent jets. *J. Atmos. Sci.*, *60*, 2101–2118, 2003.
- Feldstein, S., and S. Lee, Mechanisms of zonal index variability in an aquaplanet GCM, *J. Atmos. Sci.*, *53*, 3541–3555, 1996.
- Feldstein, S., and S. Lee, Is the atmospheric zonal index driven by an eddy feedback?, *J. Atmos. Sci.*, *55*, 3077–3086, 1998.
- Fukunaga, K., and L. D. Hostetler, The estimation of the gradient of a density function, *IEEE Trans. Info. Thy*, *IT-21*, 32–40, 1975.
- Ghil, M., and S. Childress, *Topics in Geophysical Fluid Dynamics: Atmospheric Dynamics, Dynamo Theory, and Climate Dynamics*, 485 pp., Springer-Verlag, New York, 1987.
- Ghil, M., and A. W. Robertson, Solving problems with GCMs: General Circulation Models and their role in the climate modeling hierarchy, in *General Circulation Model Development: Past, Present, and Future*, edited by D. Randall, pp. 285–325, Academic Press, San Diego, 2000.
- Ghil, M., and A. W. Robertson, “Waves” vs. “particles” in the atmosphere’s phase space: A pathway to long-range forecasting? *Proc. Natl. Acad. Sci.*, *99* (Suppl. 1), 2493–2500, 2002.
- Ghil, M., and R. Todling, Tracking atmospheric instabilities with the Kalman filter. 2. Two-layer results, *Mon. Wea. Rev.*, *124*, 2340–2352, 1996.

- Hand, D. J., H. Mannila, and P. Smyth, *Principles of Data Mining*, MIT Press, Cambridge, MA, pp. 425, 2001.
- Hannachi, A., and A. O’Neill, Atmospheric multiple equilibria and non-Gaussian behaviour in model simulations, *Quart. J. Royal Meteor. Soc.*, *127*, 939–958, 2001.
- Hansen, A. R., and A. Sutera, On the probability density distribution of planetary-scale atmospheric wave amplitude, *J. Atmos. Sci.*, *43*, 3250–3265, 1986.
- Hansen, A. R., and A. Sutera, The role of topography in the low-frequency variability of the large-scale midlatitude circulation, *J. Atmos. Sci.*, *52*, 2497–2508, 1995.
- Hartmann, D. L., and F. Lo, Wave-driven zonal flow vacillation in the Southern Hemisphere, *J. Atmos. Sci.*, *55*, 1303–1315, 1998.
- Hendon, H. H., and D. L. Hartmann, Variability in a nonlinear model of the atmosphere with zonally symmetric forcing, *J. Atmos. Sci.*, *42*, 2783–2797, 1985.
- Keppenne, C. L., S. L. Marcus, M. Kimoto, and M. Ghil, Intraseasonal variability in a two-layer model and observations, *J. Atmos. Sci.*, *57*, 1010–1028, 2000.
- Kidson, J. W., Indices of the Southern Hemisphere zonal wind, *J. Clim.*, *1*, 183–194, 1988.
- Kimoto, M., and M. Ghil, Multiple flow regimes in the Northern Hemisphere winter. Part I: Methodology and hemispheric regimes, *J. Atmos. Sci.*, *50*, 2625–2643, 1993a.
- Kimoto, M., and M. Ghil, Multiple flow regimes in the Northern Hemisphere winter. Part II: Sectorial regimes and preferred transitions, *J. Atmos. Sci.*, *50*, 2645–2673, 1993b.
- Kloeden, P. E., and E. Platen, *Numerical Solution of Stochastic Differential Equations*, 632pp., Springer-Verlag, New York, 1992.
- Kondrashov, D., S. Kravtsov, and M. Ghil, Empirical mode reduction in a model of extratropical low-frequency variability, *J. Atmos. Sci.*, submitted, 2005.
- Koo, S. Nonlinear aspects of atmospheric zonal-flow vacillation. Ph. D. Thesis, 163 pp., University of California, Los Angeles, 2002.
- Koo, S., and M. Ghil. Successive bifurcations in a simple model of atmospheric zonal-flow vacillation. *Chaos*, *12*, 300–309, 2002.
- Koo, S., A. W. Robertson, and M. Ghil. Multiple regimes and low-frequency oscillations in the Southern Hemisphere’s zonal-mean flow. *J. Geophys. Res.*, *10.1029/2001JD001353*, 2003.
- Kravtsov, S., A. W. Robertson and M. Ghil. Low-frequency variability in a baroclinic beta-channel with land-sea contrast. *J. Atmos. Sci.*, *60*, 2267–2293, 2003.

- Kravtsov, S., A. W. Robertson, and M. Ghil, Bimodal behavior in the zonal mean flow of a baroclinic β -channel model. *J. Atmos. Sci.*, accepted, 2005a.
- Kravtsov, S., A. W. Robertson, and M. Ghil, Multiple regimes and low-frequency oscillations in the Northern Hemisphere's zonal flow, *J. Atmos. Sci.*, *sub judice*, 2005b.
- Lee, S., and S. Feldstein, Mechanism of zonal index evolution in a two-layer model, *J. Atmos. Sci.*, *53*, 2232–2246, 1996.
- Legras, B., and M. Ghil, Persistent anomalies, blocking and variations in atmospheric predictability, *J. Atmos. Sci.*, *42*, 433–471, 1985.
- Lions, J. L., O. P. Manley, R. Teman and S. Wang, Physical interpretation of the attractor dimension for the primitive equations of atmospheric circulation, *J. Atmos. Sci.*, *54*, 1137–1143, 1997.
- Lorenz, E. N., 1963, The mechanics of vacillation, *J. Atmos. Sci.*, *20*, 448464.
- Lorenz, D. J., and D. L. Hartmann, Eddy-zonal flow feedback in the Southern Hemisphere, *J. Atmos. Sci.*, *58*, 3312–3327, 2001.
- Lorenz, D. J., and D. L. Hartmann, Eddy-zonal flow feedback in the Northern Hemisphere winter, *J. Climate*, *16*, 1212–1227, 2003.
- Mechoso, C., J. Farrara, and M. Ghil, Intraseasonal variability of the winter circulation in the Southern Hemisphere atmosphere, *J. Atmos. Sci.*, *48*, 1387–1404, 1991.
- Michelangeli, P.-A., R. Vautard, and B. Legras, Weather regimes: Recurrence and quasi stationarity, *J. Atmos. Sci.*, *52*, 1237–1256, 1995.
- Mo, K. C., and M. Ghil, Statistics and dynamics of persistent anomalies, *J. Atmos. Sci.*, *44*, 877–901, 1987.
- Mo, K. C., and M. Ghil, Cluster analysis of multiple planetary flow regimes, *J. Geophys. Res.*, *93*, 10927–10952, 1988.
- Namias, J., The index cycle and its role in the general circulation, *J. Meteo.*, *7*, 130–139, 1950.
- Reinhold, B. B., and R. P. Pierrehumbert, 1982, Dynamics of weather regimes: Quasi-stationary waves and blocking. *Mon. Wea. Rev.*, *110*, 1105–1145.
- Robertson, A. W., and C. R. Mechoso, 2003: Circulation Regimes and Low-Frequency Oscillations in the South Pacific Sector. *Mon. Wea. Rev.*, *131*, 1566–1576.
- Robinson, W. A., The dynamics of the zonal index in a simple model of the atmosphere, *Tellus*, *43A*, 295–305, 1991.
- Robinson, W. A., Does eddy feedback sustain variability in the zonal index?, *J. Atmos. Sci.*, *53*, 3556–3569, 1996.
- Robinson, W. A., Dissipation dependence of the jet latitude, *J. Clim.*, *2*, 176–182, 1997.

- Robinson, W. A., A baroclinic mechanism for the eddy feedback on the zonal index, *J. Atmos. Sci.*, *57*, 415–422, 2000.
- Robinson, W. A., Comments on “The Structure and Composition of the Annular Modes in an Aquaplanet General Circulation Model,” *J. Atmos. Sci.*, *61*, 949–953.
- Rossby, C.-G., and H. C. Willett, The circulation of the upper troposphere and lower stratosphere, *Science*, *108*, 643–652, 1948.
- Saravanan, R., and J. C. McWilliams, Multiple equilibria, natural variability, and climate transitions in an idealized ocean-atmosphere model, *J. Clim.*, *8*, 2296–2323, 1995.
- Silverman, B. W., *Density Estimation for Statistics and Data Analysis*, 175 pp., Chapman and Hall, New York, 1986.
- Smyth, P., K. Ide, and M. Ghil, Multiple regimes in Northern Hemisphere height fields via mixture model clustering, *J. Atmos. Sci.*, *56*, 3704–3723, 1999.
- Titterton, D. M., A. F. M. Smith, and U. E. Makov, *Statistical Analysis of Finite Mixture Distributions*, 245 pp., John Wiley and Sons, New York, 1985.
- Thompson, D. W. J., and J. M. Wallace, Annular modes in the extratropical circulation. Part I: Month-to-month variability, *J. Clim.*, *13*, 1000–1016, 2000.
- Thompson, D. W. J., J. M. Wallace, and G. C. Hegerl, Annular modes in the extratropical circulation. Part II: Trends, *J. Clim.*, *13*, 1018–1036, 2000.
- Trenberth, K. E., Short-term climate variations: Recent accomplishments and issues for future progress, *Bull. Amer. Meteor. Soc.*, *78*, 1081–1096, 1997.
- Vallis, G. K., Gerber, E. P., Kushner, P. J., Cash, and A. Benjamin, A mechanism and simple dynamical model of the North Atlantic Oscillation and Annular Modes. *J. Atmos. Sci.*, *61*, 264–280, 2004.
- Vautard, R., Multiple weather regimes over the North Atlantic: Analysis of precursors and successors, *Mon. Wea. Rev.*, *118*, 2056–2081, 1990.
- Vautard, R., B. Legras, and M. Déqué, On the source of midlatitude low-frequency variability. Part I: A statistical approach to persistence, *J. Atmos. Sci.*, *45*, 2811–2843, 1988.
- Vautard, R., K. C. Mo, and M. Ghil, Statistical significance test for transition matrices of atmospheric Markov chains, *J. Atmos. Sci.*, *47*, 1926–1931, 1990.
- Wallace, J. M., North Atlantic Oscillation/annular mode: Two paradigms—one phenomenon, *Quart. J. Roy. Met. Soc.*, *126*, 791–805, 2000.
- Wallace, J. M., and H. H. Hsu, Another look at the index cycle, *Tellus*, *37A*, 478–486, 1985.
- Webster, P. J., and J. L. Keller, Atmospheric variations: vacillations and index cycles, *J. Atmos. Sci.*, *32*, 1283–1300, 1975.

- Willett, H. C., Patterns of world weather changes, *Trans. Amer. Geophys. Union*, 29, 803–809, 1948.
- Yoden, S., M. Shiotani, and I. Hirota, Multiple planetary flow regimes in the Southern Hemisphere, *J. Meteor. Soc. Japan*, 65, 571–585, 1987.
- Yu, J.-Y. and D. L. Hartmann, Zonal flow vacillation and eddy forcing in a simple GCM of the atmosphere, *J. Atmos. Sci.*, 50, 3244–3259, 1993.

List of Figures

1	The two leading EOFs of the 10-day low-pass filtered zonally and vertically averaged zonal flow.	31
2	Data scatter in terms of leading EOFs. (a) Abscissa is the root-mean square (RMS) magnitude of anomalies in phase space computed with only PC-1, and ordinate is the RMS magnitude of anomalies with PC-2 through PC-10. (b) Abscissa is the RMS magnitude of anomalies computed with PC-1 and PC-2, and ordinate is the RMS magnitude of anomalies with PC-3 through PC-10.	32
3	Least-squares cross validation (LSCV) scores as a function of the smoothing parameter h . The scores on the ordinate are only defined up to an arbitrary constant equal to the sum of squares of the true (but unknown) PDF [see Fig. 9 and Eqs. (A.1) and (A.2) in Kimoto and Ghil (1993a)].	33
4	Estimated PDF of the zonal-flow profile. (a) Two-dimensional PDF on a plane spanned by EOF-1 and EOF-2, with a smoothing parameter $h = 0.4$; axes are scaled by the standard deviation of PC-1 and contours are increasing from 0.04 (outermost) in intervals of 0.04. The symbol '+' denotes regime centroids. (b) Number, out of 100, of random PDFs that fell short of the PDF values shown in (a). Contour interval is 10 and the regions with values larger than 95 are shaded.	34
5	Same as Fig. 4a but for the quasi-stationary (QS) dataset.	35
6	Cross-validated log-likelihood per sample as a function of the number of clusters, computed by randomly dividing the data set into two equal partitions 20 times; see Smyth et al. (1999) for details.	36
7	Mixture model estimates of regime centroids, denoted by the symbol *, and covariance ellipses, superimposed on the data scatter. Only every 50th data point has been plotted for clarity.	37
8	Composites of zonally and vertically averaged zonal-wind profiles that belong to the regime events: (a) total and (b) anomalous.	38
9	Composites of zonal mean wind at the two model levels for: (a) low-latitude and (b) high-latitude regime events.	39

10	Composite anomalies with respect to standardized regime evolution: (a) and (b) vertically averaged zonal mean wind; (c) and (d) vertical wind shear; (e) and (f) vertically averaged eddy momentum flux convergence; and (g) and (h) low-level eddy heat flux. The left panels are for the low-latitude regime and the right panels for the high-latitude regime. Regime onset and break correspond to nondimensionalized time 0 and 10, respectively. The contour interval in (a) and (b) is 1.0 ms^{-1} , in (c) and (d) is 0.5 ms^{-1} , in (e) and (f) is $2.5 \times 10^{-6} \text{ ms}^{-2}$, and in (g) and (h) is 0.5 Kms^{-1} . Solid contours are positive, dashed ones are negative, and zero contour is omitted. Shaded areas are statistically significant at the 95% level (see text for details).	40
11	Composites of a measure of acceleration of zonal mean wind, with respect to standardized regime evolution. This measure of acceleration is defined by the root-mean-square (RMS) difference between two meridional profiles, two days apart, of zonally and vertically averaged zonal wind, divided by the time elapsed. Onset and break correspond to the normalized epochs of 0 and 10 days, respectively. Dashed lines indicate a 95% confidence interval for the estimated climatological mean value of the RMS acceleration.	41
12	Dependence of the latitudinal position of the preferred regimes' zonal-jet maximum on bottom friction strength (reciprocal of Ekman drag time scale). . .	42
13	(a) Potential function used in Eq. (A1) to generate random time series. Contours are increasing from 3 (innermost one) in intervals of 3. (b) Asymptotic PDF of random time series of 200 000 samples generated from Eq. (A1) using the potential function in (a). Contours are increasing from 0.04 (outermost) in intervals of 0.04, as in Fig. 4a.	43

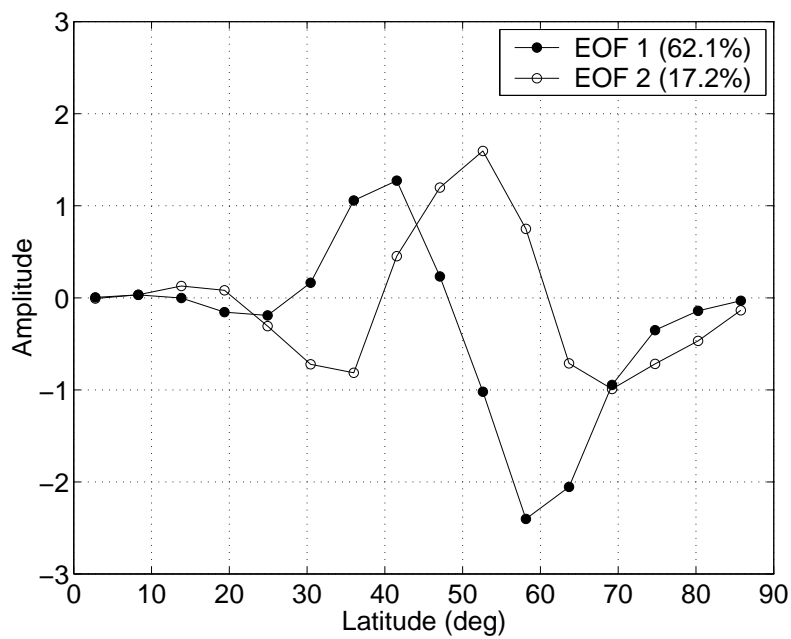


Figure 1: The two leading EOFs of the 10-day low-pass filtered zonally and vertically averaged zonal flow.

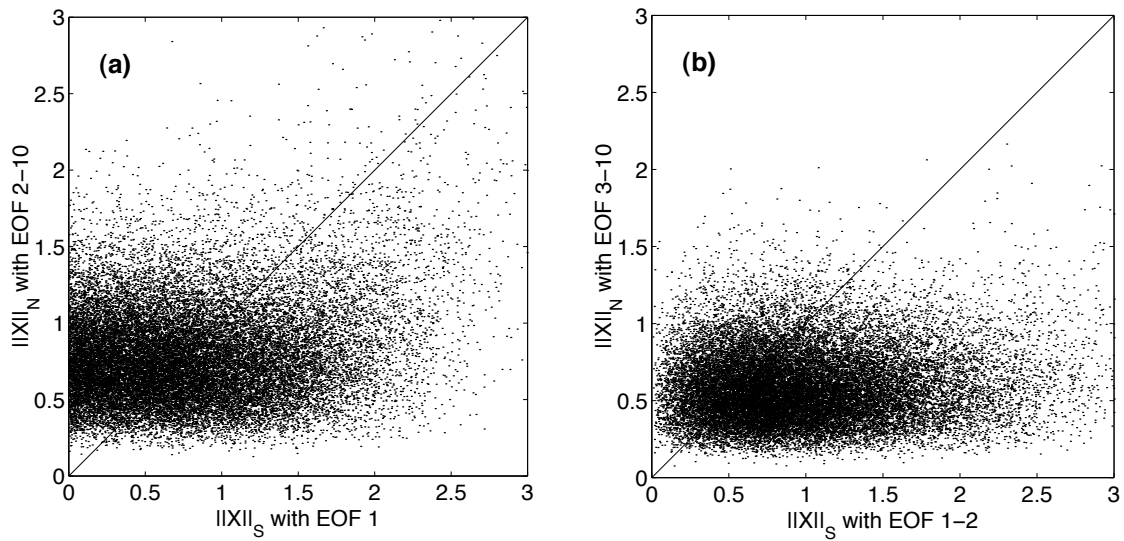


Figure 2: Data scatter in terms of leading EOFs. (a) Abscissa is the root-mean square (RMS) magnitude of anomalies in phase space computed with only PC-1, and ordinate is the RMS magnitude of anomalies with PC-2 through PC-10. (b) Abscissa is the RMS magnitude of anomalies computed with PC-1 and PC-2, and ordinate is the RMS magnitude of anomalies with PC-3 through PC-10.

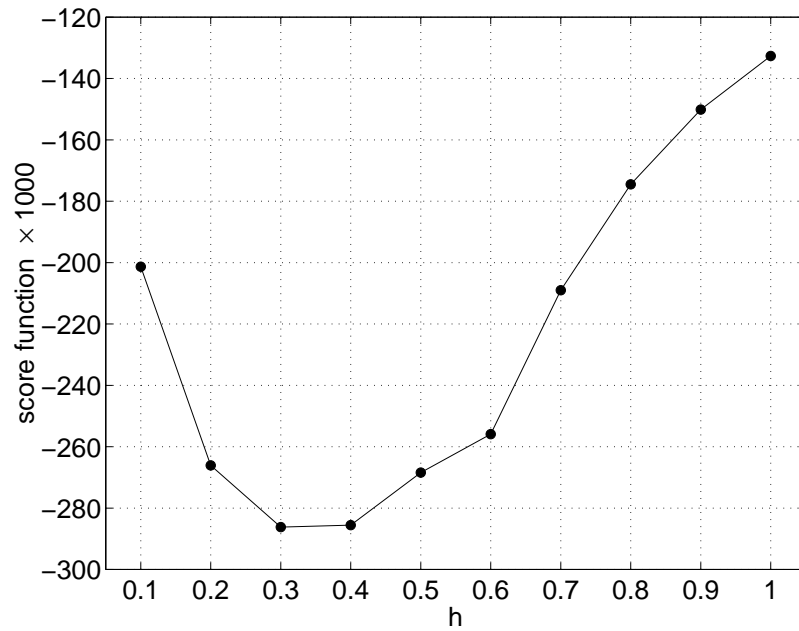


Figure 3: Least-squares cross validation (LSCV) scores as a function of the smoothing parameter h . The scores on the ordinate are only defined up to an arbitrary constant equal to the sum of squares of the true (but unknown) PDF [see Fig. 9 and Eqs. (A.1) and (A.2) in Kimoto and Ghil (1993a)].

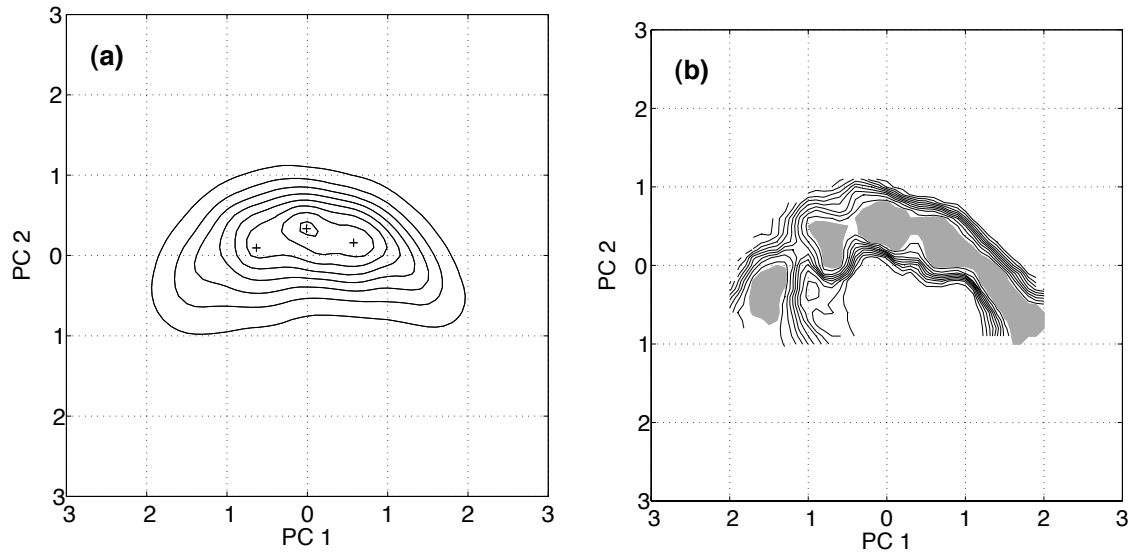


Figure 4: Estimated PDF of the zonal-flow profile. (a) Two-dimensional PDF on a plane spanned by EOF-1 and EOF-2, with a smoothing parameter $h = 0.4$; axes are scaled by the standard deviation of PC-1 and contours are increasing from 0.04 (outermost) in intervals of 0.04. The symbol '+' denotes regime centroids. (b) Number, out of 100, of random PDFs that fell short of the PDF values shown in (a). Contour interval is 10 and the regions with values larger than 95 are shaded.

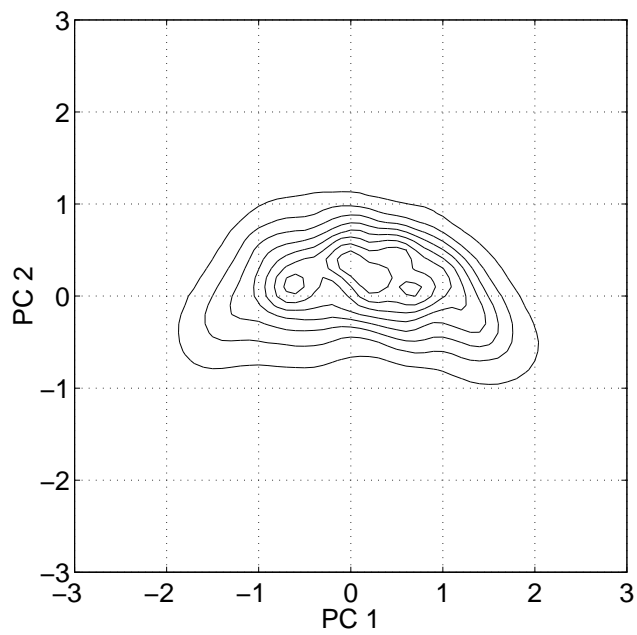


Figure 5: Same as Fig. 4a but for the quasi-stationary (QS) dataset.

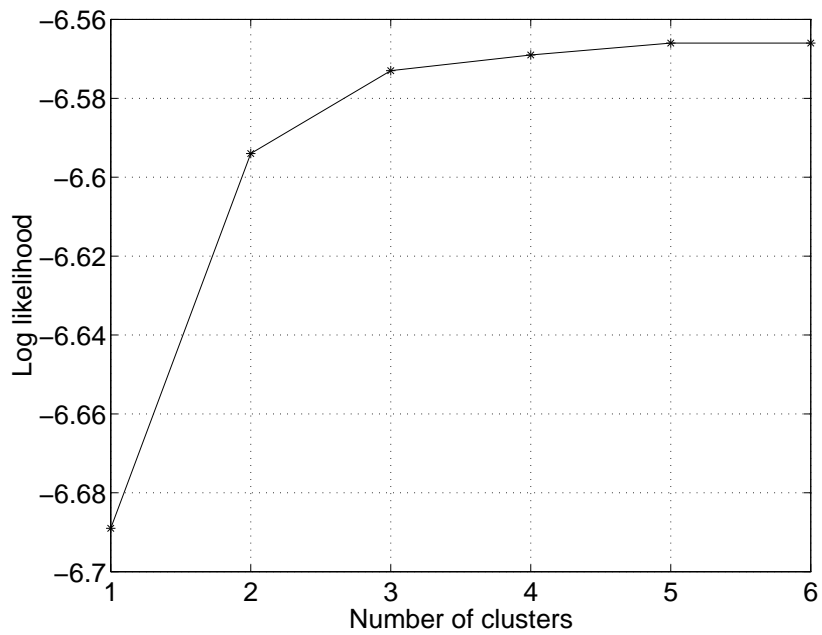


Figure 6: Cross-validated log-likelihood per sample as a function of the number of clusters, computed by randomly dividing the data set into two equal partitions 20 times; see Smyth et al. (1999) for details.

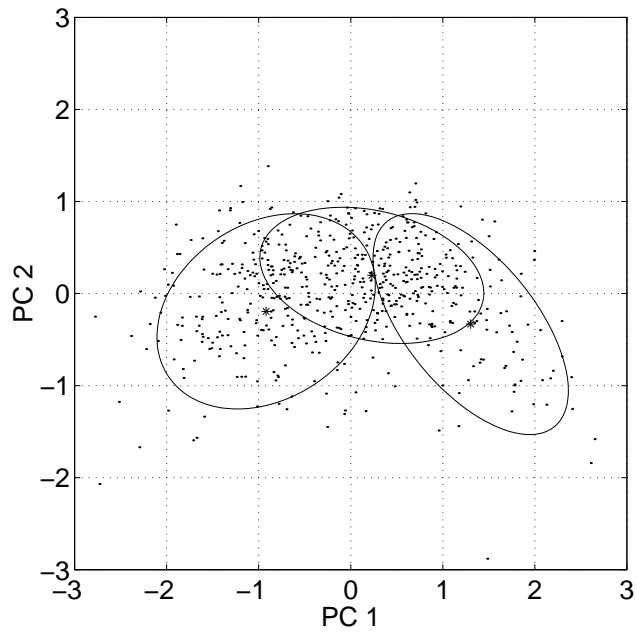


Figure 7: Mixture model estimates of regime centroids, denoted by the symbol *, and covariance ellipses, superimposed on the data scatter. Only every 50th data point has been plotted for clarity.

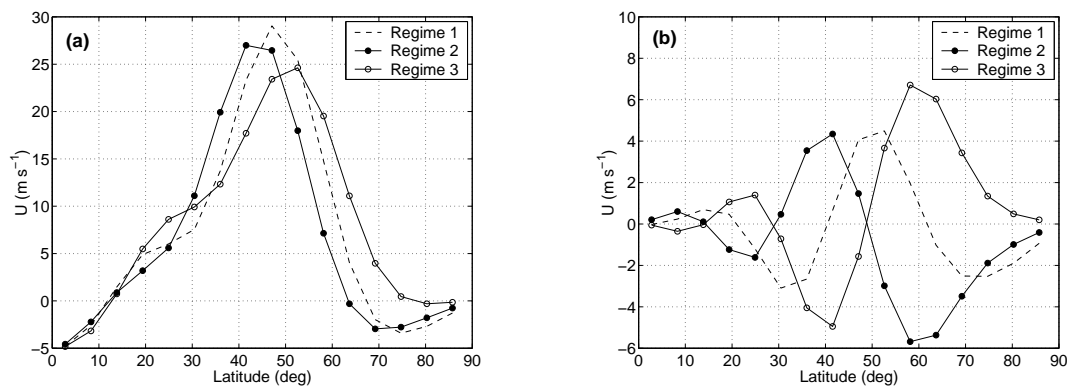


Figure 8: Composites of zonally and vertically averaged zonal-wind profiles that belong to the regime events: (a) total and (b) anomalous.

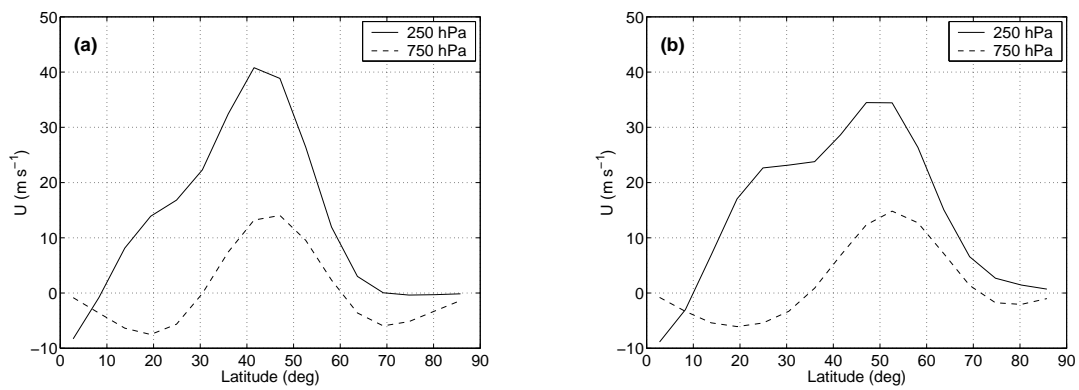


Figure 9: Composites of zonal mean wind at the two model levels for: (a) low-latitude and (b) high-latitude regime events.

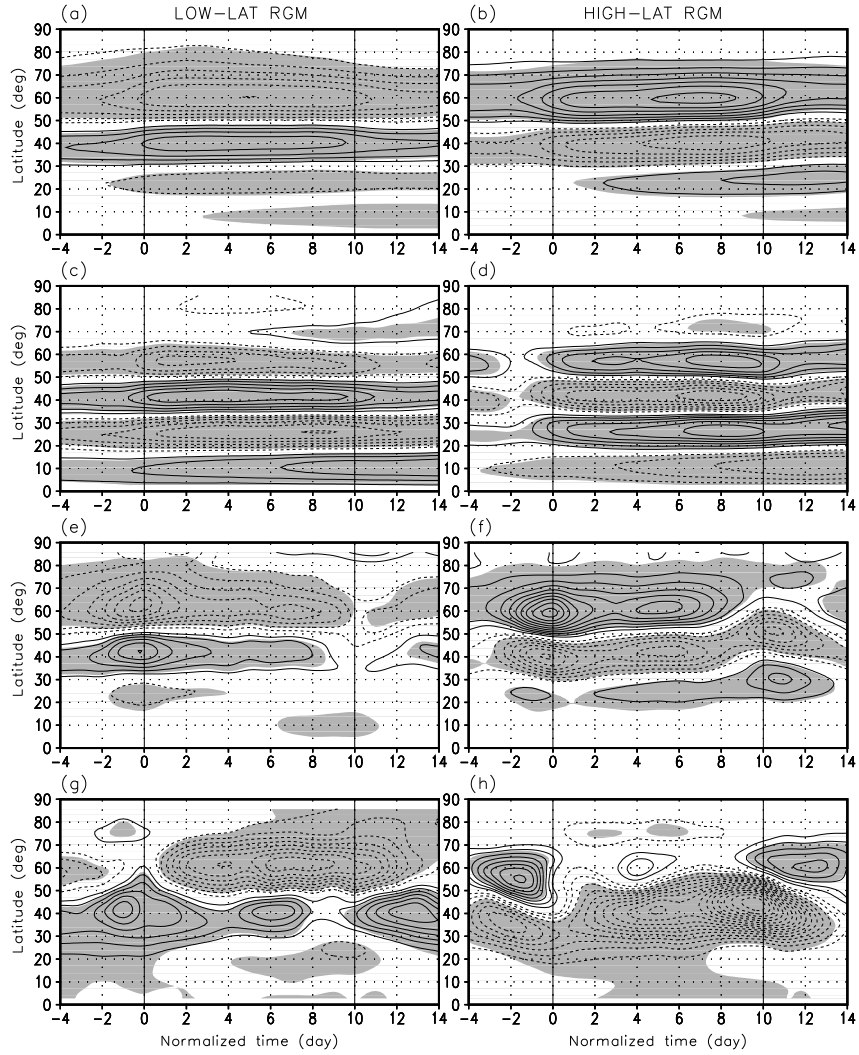


Figure 10: Composite anomalies with respect to standardized regime evolution: (a) and (b) vertically averaged zonal mean wind; (c) and (d) vertical wind shear; (e) and (f) vertically averaged eddy momentum flux convergence; and (g) and (h) low-level eddy heat flux. The left panels are for the low-latitude regime and the right panels for the high-latitude regime. Regime onset and break correspond to nondimensionalized time 0 and 10, respectively. The contour interval in (a) and (b) is 1.0 ms^{-1} , in (c) and (d) is 0.5 ms^{-1} , in (e) and (f) is $2.5 \times 10^{-6} \text{ ms}^{-2}$, and in (g) and (h) is 0.5 Kms^{-1} . Solid contours are positive, dashed ones are negative, and zero contour is omitted. Shaded areas are statistically significant at the 95% level (see text for details).

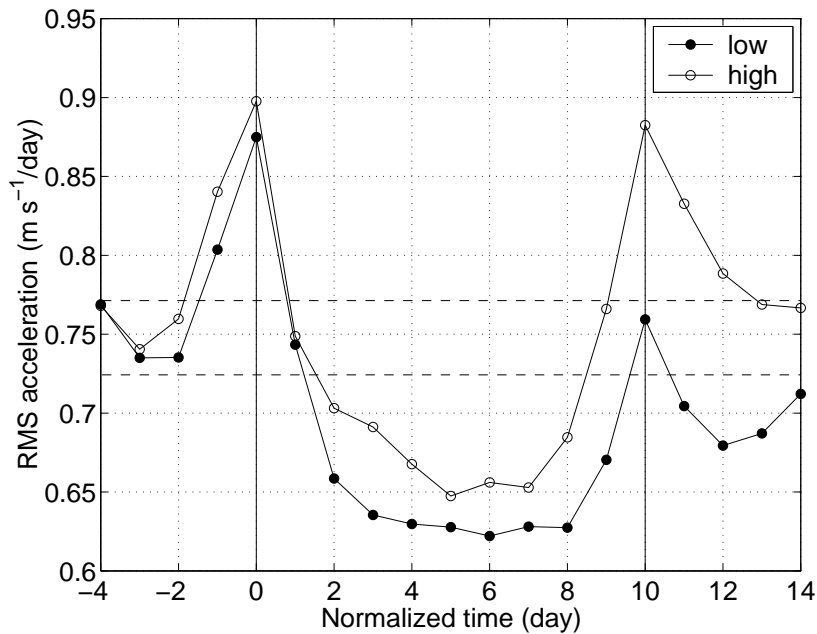


Figure 11: Composites of a measure of acceleration of zonal mean wind, with respect to standardized regime evolution. This measure of acceleration is defined by the root-mean-square (RMS) difference between two meridional profiles, two days apart, of zonally and vertically averaged zonal wind, divided by the time elapsed. Onset and break correspond to the normalized epochs of 0 and 10 days, respectively. Dashed lines indicate a 95% confidence interval for the estimated climatological mean value of the RMS acceleration.

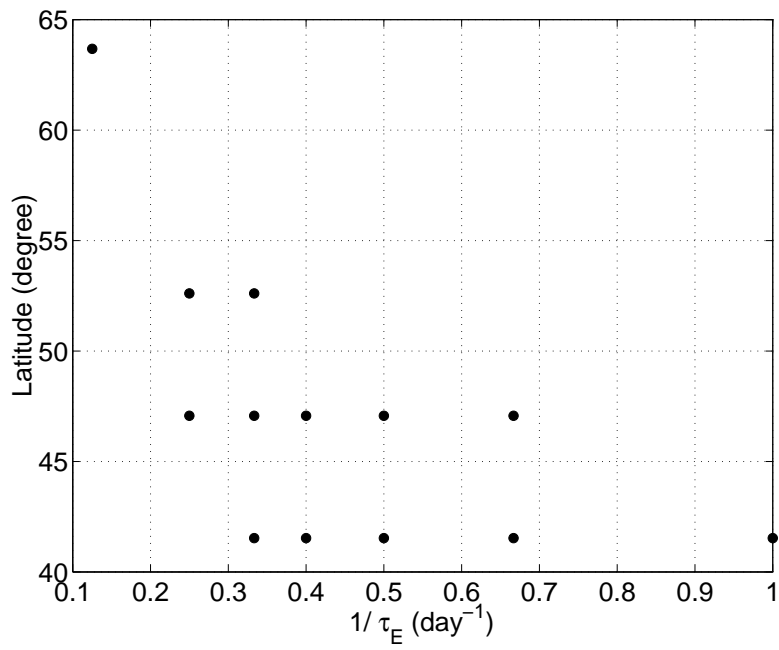


Figure 12: Dependence of the latitudinal position of the preferred regimes' zonal-jet maximum on bottom friction strength (reciprocal of Ekman drag time scale).

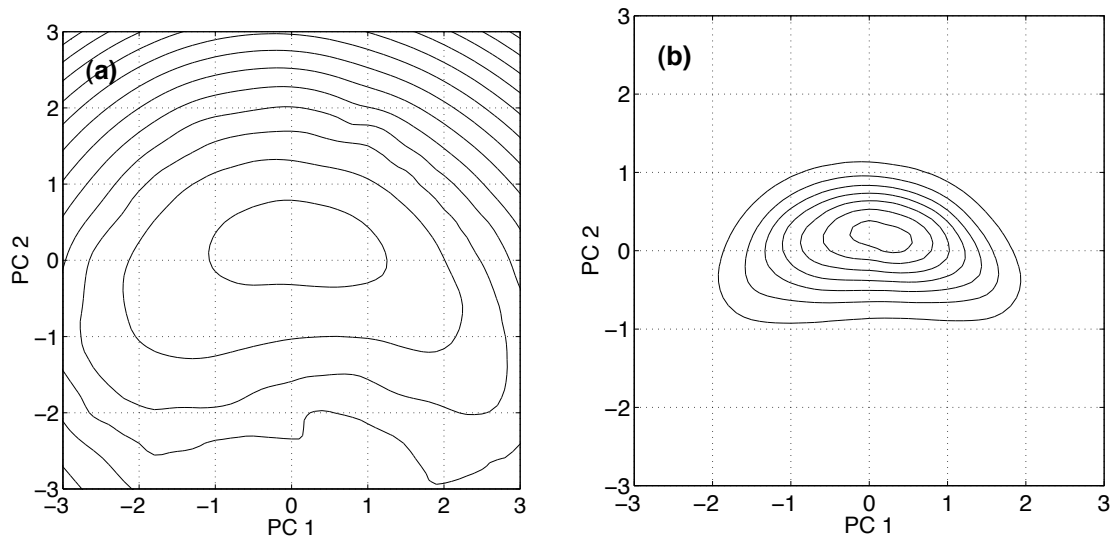


Figure 13: (a) Potential function used in Eq. (A1) to generate random time series. Contours are increasing from 3 (innermost one) in intervals of 3. (b) Asymptotic PDF of random time series of 200 000 samples generated from Eq. (A1) using the potential function in (a). Contours are increasing from 0.04 (outermost) in intervals of 0.04, as in Fig. 4a.